

Evaluation of spatial moisture distribution during CLARA 96 using spaceborne radar interferometry

Ramon F. Hanssen and Tammy M. Weckwerth

DEOS, Delft Institute for Earth-Oriented Space,
Delft University of Technology. Thijsseweg11, 2629 JA Delft, The Netherlands.
Tel: +31-(0)15-2782565, Fax: +31-(0)15-2783711, e-mail: hanssen@geo.tudelft.nl
NCAR, National Center for Atmospheric Research, Boulder, CO, 80307-3000 USA.
Tel:+1 303-4978790, Fax:+1-303-4972044, email: tammy@atd.ucar.edu

Recent experiments have shown that spaceborne radar interferometry can be used to infer atmospheric parameters at a spatial resolution of 20 m based on very high accuracy integrated refractivity measurements [1]. In this application, the signal delay of the pulses from Synthetic Aperture Radar (SAR) is used, acquiring images over a swath width of 100 km. It is possible to extract signal delay differences between pixels in SAR data using the coherent summation of the phase information in two SAR images, acquired with a 1 day interval. Tropospheric signal delay at C-band radar is a line-of-sight integration over the refractivity of the medium, which is determined by pressure, temperature, humidity, and, to less extent, liquid water droplets. The obtained radar interferogram is a double difference measurement; spatial delay differences obtained during two SAR acquisitions are differenced in time. As the interferogram is inherently relative, parameters, which vary only slightly over the scene, are of less importance when compared to highly variable components. It can be shown that the dominant part of the signal in the radar interferogram is caused by the atmospheric water vapor distribution.

In this study a specific interferogram will be analyzed, acquired at 23 and 24 April 1996 over the southwestern part of the Netherlands, see fig. 1. The two SAR acquisitions coincide with the 'Clouds and Radiation' (CLARA) experiment, which is aimed at a better understanding of the interaction between clouds and radiation by improving the measurement of cloud properties [2]. Since the development of clouds is highly influenced by the water vapor distribution, the SAR data can be used to estimate the precipitable water content of clouds relative to the ambient environment. The high resolution of the data reveals regions of enhanced moisture leading to cloud formation and rain.

Similar space-geodetic techniques, such as GPS, are influenced in nearly the same way as SAR. Therefore, these data are used to describe the tropospheric situation during the experiment and identify specific features in the interferogram, in combination with an extensive array of supporting instrumentation. A statistical evaluation of the dataset is presented using two-dimensional structure func-

tions, and conclusions on the potential and limits of radar interferometry as a meteorological technique are discussed.

METHODOLOGY

For a general introduction to radar interferometry, a discussion of system characteristics and geophysical applications can be found in [3] and [4]. First results on the atmospheric application of the technique are given in [1] and a background of the derivation of precipitable water vapor (PWV) for radar interferometry can be found in [5]. This paper is limited to the analysis and interpretation of one specific interferogram. This radar interferogram is the coherent complex multiplication of two SAR acquisitions. At 23 April 1996, 10:38:07 UTC (12:38:07 Local Time), the active microwave instrument on-board ERS-1 acquired frame 2565 during orbit 24960, covering an area of 100x100 km. The phase information in this complex dataset consists of (1) geometric path length differences between the radar antenna and all pixels at the earth's surface, (2) the additional delay of the signal due to spatial refractive index variations in the atmosphere, and (3) uniformly distributed random noise due to the unknown surface scattering characteristics. Due to the latter component, the first two are effectively masked by noise. As a result, it is not possible to retrieve the atmospheric delay component. Exactly 24 hours later, the twin instrument on-board ERS-2, orbit 5287, acquired the same part of the earth's surface, from a nearly identical position as ERS-1 one day before. Both satellite positions differ only 38 m in the oblique look direction of the radar, and 78 m perpendicular to the look direction. From an altitude of 785 km, the difference in viewing geometry between both satellites is negligible. As a result, the third phase component, due to surface scattering, is identical during this second acquisition, apart for some unknown bias. Over water areas, surface scattering is different for both acquisitions and no useful phase information can be derived.

After exact alignment, the second phase image is subtracted from the first by complex multiplication to obtain the phase-difference image or interferogram. Here, the phase information is caused by the superposition of the

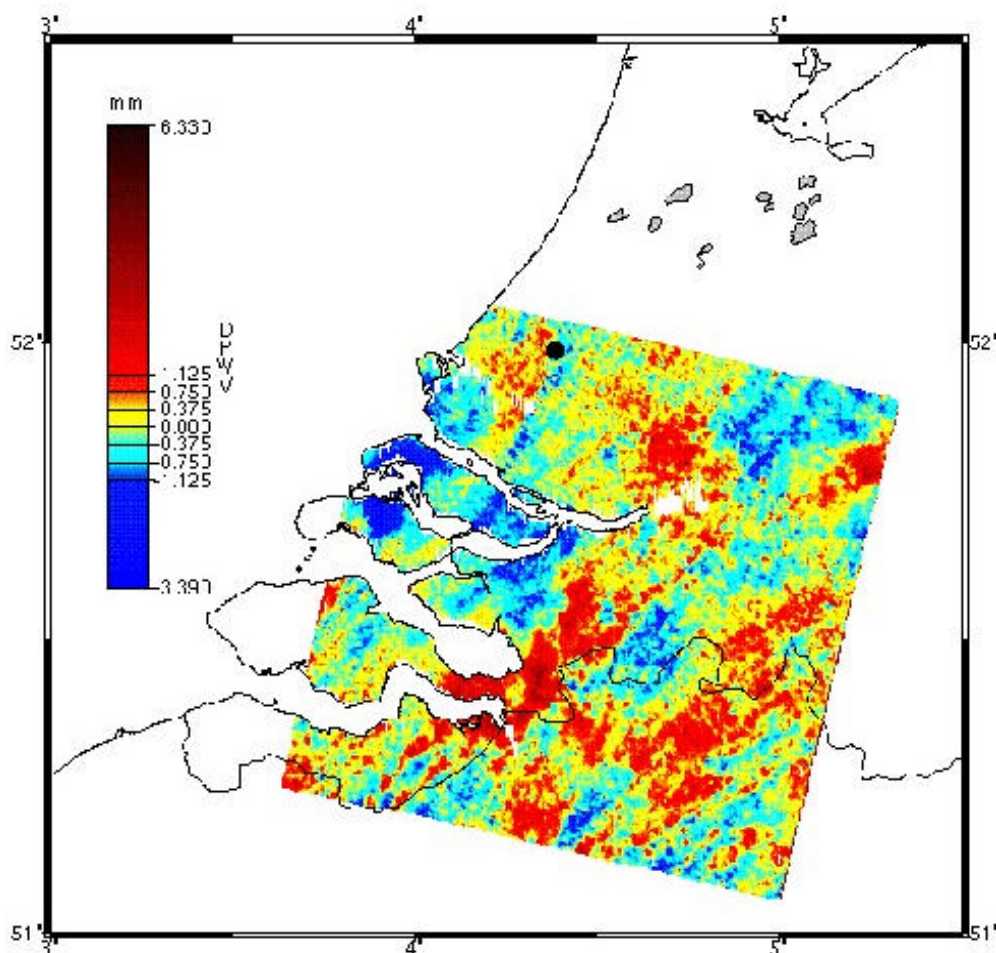


Fig.1. Differential SAR interferogram of 23 and 24 April 1996 10:38 UTC using a Mercator projection and WGS84 coordinates. All topographic information has been removed using a reference elevation model. The interferometric phase has been converted to zenith delay differences with zero – average and subsequently to differential precipitable water vapor (DPWV) using a mean surface temperature of 15.1°C [9]. The colorbar is linear between –1.5 and 1.5 mm. Bluish colors correspond with signal on 23 April, while red-yellow regions are related to 24 April. The black dot indicates the position of Delft, where most CLARA in situ observations were performed.

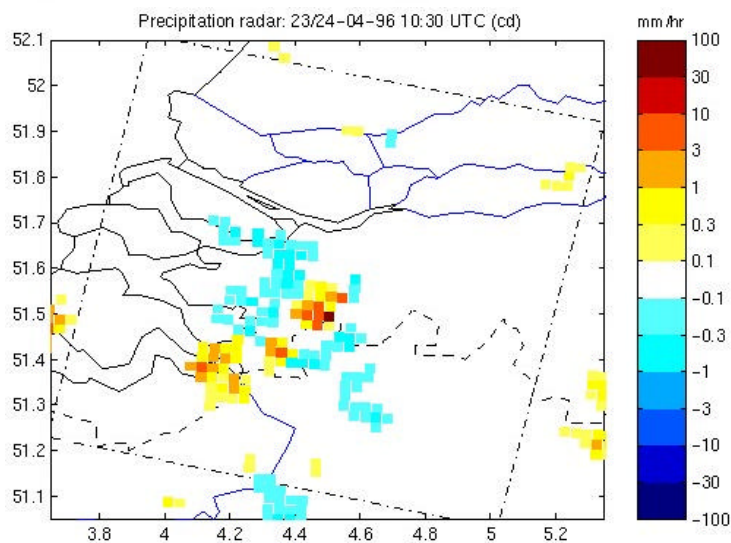


Fig.2. Weather radar reflectivity of 23 and 24 April, 10:30 UTC, converted to rain rate in mm/h. The data of the two days are superposed in one image using negative values for 23 April and positive values for 24 April. Comparison with fig.1 shows that rain areas correspond with strong values for DPWV in the interferogram. This, however, does not hold the other way around, e.g.; at (4.0°, 51.75°) a strong anomaly during 23 April is not connected to rainfall.

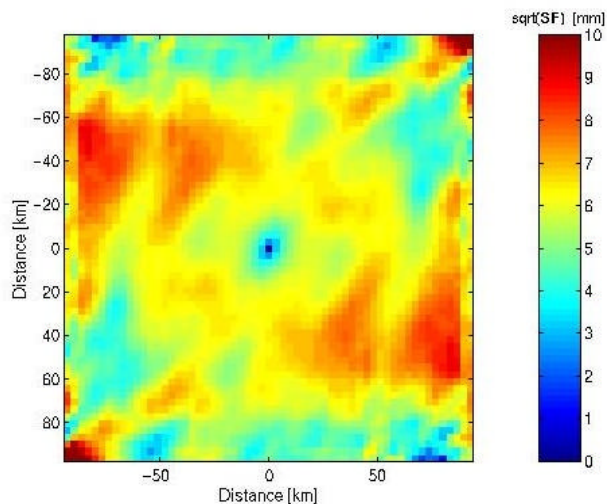


Fig.3. Two-dimensional structure functions derived from the original interferogram converted to delay observations. The square-root of the structure function values are displayed to simplify interpretation of the delay differences. For every combination (dx, dy), the standard deviation of the difference between two pixels is shown. The 2D structure function is symmetric around the origin.

two geometric components and the two delay components. Using a reference elevation model for the test area, it is possible to extract both geometric terms, which yields a differential interferogram. In this image, phase differences are only due to atmospheric delay and long wavelength trends due to orbit inaccuracies. The latter can be approximated using the variance in the orbital state vectors and tie-points at the surface. In this procedure, all long wavelength (>200 km) atmospheric information is effectively eliminated. The residual differential interferogram can be regarded as an 'atmosphere-only' image.

Phase differences in the differential interferogram need to be interpreted with some precaution. First, it is important to realize that the interferogram only contains relative phase information. There is no absolute calibration point. As a result, the value of one single pixel is useless. Second, the variation of the phase is due to the spatial variability during *two* acquisition times with a different state of the atmosphere. This ambiguity is a limiting factor for data interpretation if only two SAR images are used, as in this study. Using a number of SAR images, interferograms can be made between different combinations, which enables one to overcome this ambiguity. For this study, the sign of the phase values is used to attribute the phase effect to the SAR image of 23 April or 24 April. This approach can be used for strong disturbances---for small phase variation it is not possible to attribute it to one specific acquisition using only two images.

The following step in data processing is to derive slant delay differences from the phase differences. This conversion is simply performed by

$$\mathbf{d}(i, j) = \frac{I}{4p} \mathbf{j}(i, j)$$

where I is the radar wavelength (5.66 cm), $\mathbf{j}(i, j)$ is the interferometric phase value at pixel coordinates (i, j) , with $E\{\mathbf{j}\}=0$, and $\mathbf{d}(i, j)$ is the relative slant delay. Conversion to zenith delays is performed using a simple $\cos q$ mapping function, where q is the incidence angle. Since $20 < q < 23$, no ray-bending effects need to be considered.

Assuming smooth lateral pressure and temperature variation over scales less than 50 km, the observed delay variation is mainly due to variations in the wet part of the refractivity. Using the method proposed by [6] precipitable water variations, labelled differential precipitable water (DPWV), are derived from the delay interferogram and surface temperature measurements (see [5] for the derivation).

After geocoding the DPWV map from radar coordinates to the WGS84 ellipsoid, the result is shown in fig.1.

To validate the meteorological interpretation of the DPWV map, additional datasets from the CLARA experiment are used. GPS zenith delay observations, radiosonde profiles, lidar, infrared and microwave radiometer data were available at Delft, indicated by the black dot in fig. 1.

Additional Meteosat and NOAA-AVHRR data were used for comparison as well.

For the analysis of the spatial variability of the delay or water vapor signal, the two-dimensional structure function, D_δ , defined as

$$D_d(dx, dy) = \langle [\mathbf{d}(x + dx, y + dy) - \mathbf{d}(x, y)]^2 \rangle,$$

is used. Here, \mathbf{d} is the zenith delay signal and dx and dy are the distance between two arbitrary points in km. The structure function is the expectation value of the squared difference between two points at a certain distance R and azimuth α in the image. It exists for all random functions with stationary increments [7].

RESULTS

In this section a first interpretation of the interferogram is made, followed by the general meteorological interpretation of both days using the existing CLARA ground truth data. Then, a comparison with the GPS data and a statistical evaluation is performed.

Interferogram interpretation

Figure 1 shows the differential PWV map for 23 and 24 April 1996. The colorbar is linear between -1.5 and 1.5 mm in order to use the full color resolution and suppress the effect of a few localized points with very high values. The yellow-red range of the colorbar corresponds with delay signal on 24 April, blue shades correspond with 23 April. The variation can be interpreted as due to water vapor and clearly indicates bandedness along the wind direction on 24 April: SW--WSW. In the lower left part of the DPWV map, it can be observed that moisture converges into linear bands, which expand to the large anomaly at $(4.3^\circ, 51.4^\circ)$. The value and shape of this anomaly indicates a deeper column of moist air, which is expected for cumulus--cumulonimbus clouds and for regions that are penetrated by precipitation. In those sub-cloud regions, the relatively dry air will become saturated by evaporating liquid particles. Although it is in general not possible to determine whether precipitation occurs from the interferometric data only, localized showers often give a strong signal. The shape and magnitude of the anomalies suggest very localized concentrations of water vapor, as expected for convective weather with developing cumulus clouds.

The blue regions, e.g., at $(4.0^\circ, 51.8^\circ)$ and $(4.7^\circ, 51.5^\circ)$, corresponding to 23 April also indicate strong concentrations of water vapor. The existence of clouds in the area is very likely, although probably with less variation, i.e., more uniform, than at 24 April.

In fig. 2, the weather radar reflectivity of both days, 10:30 UTC, is shown, converted to rain rate in mm/h. To facilitate comparison with the interferogram, precipitation during 23 April is plotted using negative (blue) colors, and

precipitation during 24 April using positive (yellow) colors. For the grid points where precipitation occurred during both days, the average value is shown. The correlation between the precipitation regions and large DPWV values is remarkable, although the absence of precipitation at (4.0°, 51.8°) supports the hypothesis that the DPWV signal can be caused by towering cumulus alone.

General interpretation based on additional data

According to the weather maps of 23 April, a cold front has just passed over the interferogram area during the SAR acquisition. There is no obvious frontal passage signature in neither the satellite imagery nor the Delft soundings nor the Delft surface measurements of temperature, humidity, or pressure, thus the cold front was very weak. Behind it, there are isolated showers in a neutral atmosphere, as derived from weather radar and soundings. Cloud base is 2 km, as determined from the infrared radiometer cloud base temperature of 5°C which corresponds to 2 km on the sounding. The radiosonde data reveal strong winds, 10-15 m/s, from SSW. Cloud types are a combination of stratocumulus and cumulus. Near the time of the frontal passage at Delft, there were more clouds and they were more continuous (determined from liquid retrieval of microwave radiometer; also IR radiometer shows continuous cloud cover) and there was a maximum in water vapor. Then cloud cover diminished as the water vapor amounts decreased.

During the acquisition of the second SAR image, at 24 April, there were more isolated showers, but not as many as during the first day. The radiosonde observations indicate a more stable atmosphere with colder, drier air at the surface. The cloud base is 2500 m (determined from the ESTEC lidar) which is consistent with the IR radiometer cloud base temperature of -10°C and sounding temperature at this height of about -6°C. The cloud cover is thin and broken, and consists of mostly cumulus, as indicated by the IR radiometer, the ragged look of the liquid water retrieval from the microwave radiometer, and the order of magnitude less in liquid water content from the microwave radiometer on 24 April compared with 23 April. Winds are weaker during this day, 8-10 m/s, from WSW. Cloud streets, mainly developing cumulus, are visible over the interferogram area in the Meteosat double visual image at 10:30 UTC.

Comparison between SAR and GPS data

GPS observations were performed at station Delft during the two days of the interferogram. In fig. 4, the derived zenith wet delay is shown using a 6-min sampling interval. Hydrostatic delay components are removed using surface pressure data. Two pairs of vertical lines indicate an interval of 2.45 hours around the SAR acquisitions. This inter-

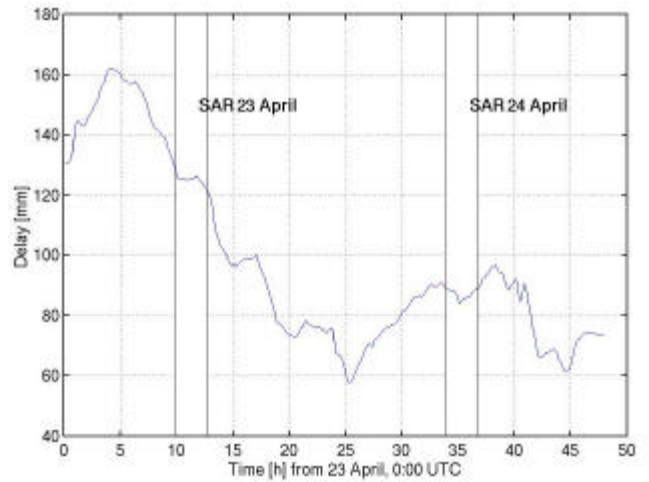


Fig.4. GPS zenith wet delay variation from 23 April, 0:00 UTC to 24 April 23:51 UTC. The vertical lines indicate two intervals of 2.45 hours, centered around the SAR acquisitions.

val was determined from an average wind speed of 10 m/s and the interferogram size of 100 km.

From the signal variation within these two intervals, it is expected that the signal variation in the interferogram is less than 15 mm. However, the zenith wet delay variation in the interferogram has a range of 54 mm. Table 1 lists some statistical values for SAR and GPS.

From figure 4 and table 1 it is obvious that a comparison between 24 hours of GPS data and the interferometric data is not possible, as the daily variation in wet delay is much stronger than the variation over a short interval. This behavior is also expected from power law considerations. On the other hand, only evaluating the 2.45 hours observations centered around the SAR acquisition time is not representative as well, as it seems to underestimate the amount of variation.

For the RMS of the zenith wet delay variation in one SAR image, it is assumed to be equal to the variation in the interferogram divided by $\sqrt{2}$, or 3.7 mm.

	Mean	RMS	Range
GPS 23 Apr 96	117.4	30.4	89.1
GPS 24 Apr 96	78.8	10.7	39.1
GPS 23 – 24	38.7	31.0	87.9
SAR	0.0	5.3	54.8

Table 1. Basic statistics for the zenith wet delay derived from the two GPS days (24 hour interval), the difference between GPS at day 23 and 24, and the SAR interferogram (instantaneous) [mm].

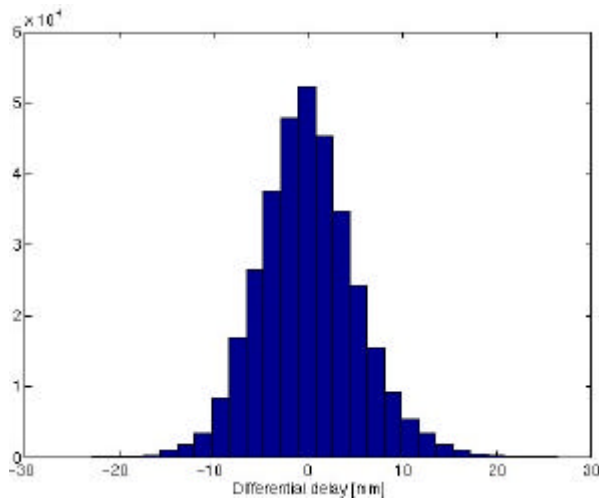


Fig. 5. Histogram of the differential delay in the interferogram showing Gaussian characteristics. Assuming the same delay characteristics at both days, the interferogram standard deviation of 5.3 mm (delay signal) corresponds with 3.7 mm during one SAR acquisition.

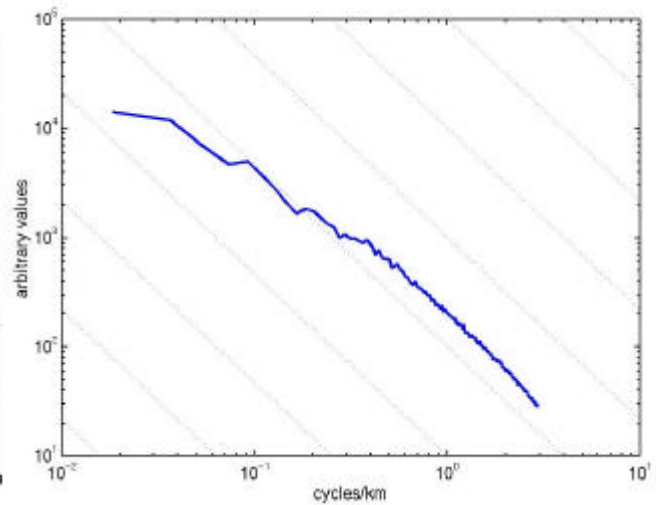


Fig. 6. One-dimensional amplitude spectrum of the interferogram showing the decrease in signal amplitude for decreasing wavelengths. The spectrum is a rotational average of the 2D amplitude spectrum. The diagonal lines indicate the typical $-5/3$ power law decay.

Regarding the spatial resolution of the GPS zenith delay observations, two remarks need to be made. First, for a cloud base at 2 km and a 20° elevation cut off, the diameter of the GPS cone at that altitude is 11 km. If an array of GPS receivers would be installed with a 11-km posting, independent observations would be guaranteed at that altitude. From Shannon's sampling theorem it follows that water vapor signal with a wavelength of 22 km or less will be aliased into the longer wavelengths. For the SAR-derived spatial delay field, using a spatial averaging to 160 m, the observations can be considered independent. On the other hand, for wavelengths larger than, say 50 km, gradient errors due to satellite orbit inaccuracies and hydrostatic effects limit the unambiguous interpretation of the signal. Such considerations can be important when an array of GPS receivers is available.

Secondly, in the case where only one GPS receiver is available, the temporal behavior of the signal might give a first indication of the delay variability. To perform the conversion from temporal to spatial information, a 'frozen' boundary layer is assumed in which the anomalies do not develop but are only transported in their original shape by the wind. With this rather stringent assumption, the wind speed is needed for the conversion. The observed wind speed during 23 April is approximately 10 m/s. With the 11-km diameter of the GPS observation cone at 2-km alti-

tude, the sampling interval should be 18 minutes to interpret the observations as independent. The 6-10 min sample interval used during the CLARA experiment is therefore clearly too short to interpret the short-wavelength signal. For a comparison with the SAR observations, the sampling interval of 20 min should be used, which results in a shortest wavelength of 40 min, or 24 km.

Scale dependent statistics

For the description of boundary layer turbulence characteristics as well as analyzing the geodetic implications of positioning using space-geodetic methods, the spatial behavior of the delay variation is very important. For the relative radar interferogram the first moment or expectation value of the delay is zero. In fig. 5, the histogram of the delay data from the interferogram is displayed. The second moment or dispersion of single observations can be derived but is less interesting as the dispersion of increments. The latter can be described by analyzing the power or the magnitude spectrum or by the structure function and reveals information on the drop-off of power for smaller spatial increments. Fig. 6. is the rotationally averaged amplitude spectrum of a continuous part of the interferogram. It is derived by computing the 2D FFT and averaging all values with the same radial distance to the origin. The diagonal

lines indicate the typical $-5/3$ power law decay for higher frequencies. For wavelengths between 0.5 and 2.5 km the variation clearly follows the $-5/3$ decay. A small deviation at 2.5-km (0.4 cycles/km) could indicate the effective height of the boundary layer in which 3D turbulence characteristics play a dominant role. For longer wavelengths, the decay is less strong, as expected for effective 2D turbulent characteristics.

The two-dimensional structure function $D_8(dx,dy)$ reveals information on the correlation of single pixels with other pixels in the image. In fig 3., the square root of the structure function is shown. The non-isotropy of the field can be clearly derived, in this case mainly caused by the two strong delay signatures in separate acquisitions. As the image is derived from averaging all combinations of pixels, there are less realizations available for the edges and corners of the image. Therefore, areas outside 70 km from the origin need to be interpreted with care. For geodetic applications, it is important to increase the variance of phase difference measurements with increasing distance.

DISCUSSION AND CONCLUSIONS

Radar interferometric data can be used to obtain a relatively accurate and high-resolution interpretation of the state of the boundary layer. Of all the observational datasets available for the CLARA project, none of them give a two-dimensional spatial overview. Weather radar gives a spatial view only if precipitation occurs, while Meteosat and NOAA-AVHRR lack resolution to observe the fine details in water vapor. All other instrumentation is situated at a single point and gives temporal or vertical information. Therefore, the radar interferograms add considerable complementary value in terms of high resolution and quantitative information. A big disadvantage of many new sensors (e.g., water vapor DIALs) is that they do not work in cloud. Therefore, radar interferometry has an advantage there as well. In the scientific community there is strong interest in water vapor measurements within clouds [8]. There may be supersaturation or subsaturation within clouds which affects droplet size distribution and particle type and therefore the radiation. With existing instrumentation, this is very difficult to determine. Nevertheless, major drawbacks are currently in the unambiguous interpretation of two superposed atmospheric situations. With only two SAR images to form one interferogram, this will be a limiting factor. Suitable SAR platforms with more frequent revisit times are expected to solve this problem. Moreover, design considerations might result in, e.g., larger swath widths or reduced resolution to speed up data processing.

Acknowledgements We gratefully acknowledge the participating institutes of the CLARA experiment for making the data set available. The European Space Agency provided the ERS SAR data. A. Feijt of KNMI provided valuable help in the data handling and interpretation.

LITERATURE

- [1] Hanssen, R.F., T.M.Weckwerth, H.A.Zebker, R. Klees, High-resolution water vapor mapping from interferometric radar measurements, *Science*, 283,1295-1298, 1999.
- [2] van Lammeren, A.C.A.P., H.W.J. Russchenberg, A.Apituley, H.ten Brink, CLARA: a data set to study sensor synergy, in *Proceedings Workshop on Synergy of Active Instruments in the Earth Radiation Mission, 12-14 Nov, Geesthacht, Germany*, ESA EWP 1968 or GKSS 98/eE10, 1997
- [3] Bamler, R., and P.Hartl, Synthetic aperture radar interferometry, *Inverse Problems*, 14, R1-R54, 1998
- [4] Massonnet, D., and K.L.Feigl, Radar interferometry and its application to changes in the earth's surface, *Reviews of Geophysics*, 36, 441-500, 1998.
- [5] Hanssen, R., *Atmospheric heterogeneities in ERS tandem SAR interferometry*, DEOS Report no 98.1, Delft University Press, Delft, the Netherlands, 1998.
- [6] Bevis, M.,S.Businger, T.A.Herring, C.Rocken, R.A.Anthes, R.H.Ware, GPS Meteorology: Remote sensing of atmospheric water vapor using the Global Positioning System, *Journal of Geophysical Research*, 97, 15787-15801, 1992
- [7] Monin, A.S. and A.M. Yaglom, *Statistical fluid mechanics: Mechanics of Turbulence*, vol. 2, MIT Press, Cambridge, 1975.
- [8] Weckwerth, T.M., V.Wulfmeyer, R.M.Wakimoto, R.M.Hardesty, J.W.Wilson, R.M.Banta, NCAR/NOAA lower-tropospheric water vapor workshop, *BAMS*, 1999, in press.